One-Structure-Based Multi-Effect Coupled Nanogenerators for Flexible and Self-Powered Multi-Functional Coupled Sensor Systems

Authors

Kun Zhao[1,4], Bangsen Ouyang[1,4], Chris R. Bowen[2], Zhong Lin Wang[1,3,4*] and Ya Yang[1,4,5*]

Affiliations

[1]CAS Center for Excellence in Nanoscience, Beijing Key Laboratory of Micro-nano Energy and Sensor, Beijing Institute of Nanoenergy and Nanosystems, Chinese Academy of Sciences, Beijing 100083, P. R. China.

[2]Department of Mechanical Engineering, University of Bath, BA2 7AK, UK

[3]School of Material Science and Engineering, Georgia Institute of Technology, Atlanta, GA 30332-0245, USA.

[4]School of Nanoscience and Technology, University of Chinese Academy of Sciences, Beijing, 100049, P. R. China.

[5]Center on Nanoenergy Research, School of Physical Science and Technology, Guangxi University, Nanning 530004, PR China.

[*]Corresponding author. Email: yayang@binn.cas.cn, zhong.wang@mse.gatech.edu

Abstract

The simultaneous monitoring of multi-physical signals is essential for future sensor systems, but is currently only realized by integrating a variety of sensor types into a single device. However, the ability to use a single sensor structure that shares common electrodes can provide a route to multi-functional sensing while also decreasing device size and increasing spatial resolution. Here we report a ferroelectric barium titanate film-based multi-effect coupled nanogenerator for scavenging light, mechanical, and thermal energies to realize a self-powered multi-functional coupled sensor system without using any external power source. The coupled nanogenerator exhibits a strong coupling enhancement with detection sensitivities of 0.42 nA/(mW/cm^2) during illumination by 405 nm light, 1.43 nA/kPa for pressure detection, and -8.85 nA/K for temperature sensing, where both the light and pressure sensing performances have the highest sensitivities during a cooling temperature variation of ~19.5 K and the largest temperature detection sensitivity can be achieved during strong light illumination of 83.2 mW/cm^2. Moreover, the coupled nanogenerator array can be integrated into flexible forms for tactile pressure, temperature, and light sensors, and enabling coupled sensing for the development of electronic skins.

MAIN TEXT

Introduction

With the rapid development of self-powered micro/nanosystems, a variety of nanogenerators based on a range of mechanisms have been widely investigated for scavenging waste energy in the environment. Examples include photovoltaic cells for scavenging solar energy (*1-5*), piezoelectric nanogenerators for scavenging mechanical energy (*6-11*) and pyroelectric nanogenerators for scavenging thermal energy (*12-16*). Such investigations are important for developing new multi-effect coupled energy materials and exploring the possibility for exploiting coupling effects between different physical properties in the same device structure. Barium titanate (BTO) is a lead-free ferroelectric with an intrinsic spontaneous polarization and demonstrates excellent pyroelectric (*17, 18*) and piezoelectric effects (*19-21*), which leads to the generation of charge when subjected to temperature variations and pressures, respectively. Its ferroelectric photovoltaic effect has also been utilized to scavenge solar energy (*22-24*). However, the majority of investigations are focused on the development of individual energy harvesters and there have been limited reports on a coupled nanogenerator based on a single structure of BTO to simultaneously scavenge the three energy sources of light, mechanical and thermal energies for self-powered coupled sensor systems. It is necessary to understand the coupling relationships between the different energy scavenging mechanisms and also the effect of coupling on the overall performance of self-powered sensors. Moreover, most of the multi-functional sensor systems are based on the simple integration of individual sensors with different functions due to the possible interactions of the devices. However, the increased cost and increased volume of such multi-device sensor systems limits their application. As a result, the development of a one-structure-based multi-functional coupled sensor system can effectively solve this issue by identifying the detailed coupled relationships between the different sensors.

Here, we report on a one-structure-based nanogenerator that couples photovoltaic, piezoelectric and pyroelectric effects for scavenging 405 nm light, mechanical and thermal energies simultaneously. When subjected to light with an intensity of 83.2 mW/cm^2, the coupled current of the nanogenerator under the application of simultaneous illumination and pressure (7.6 kPa) can be enhanced by approximately 387.3 % when compared with the output current of the device under light illumination only. When subjected to a temperature decrease of ΔT = -19.5 K, the output current signal can be enhanced by more than 375.0 % when illuminated at an intensity of 83.2 mW/cm^2. In addition, the coupled nanogenerator demonstrates excellent stability in terms of output current and exhibits no observable deviation over 100 cycles. Finally, the coupled

nanogenerator was deployed in a self-powered multi-functional coupled sensor systems for monitoring light, pressure and temperature variations. Our sensor system stands out among present multi-functional sensor systems (25, 26), since a single pixel of our sensor system can simultaneously detect light, pressure and temperature variations which can significantly improve the integration level and reduce cost. When the sensor system is deployed as a 3×3 sensor array, it can successfully detect the distribution of light, pressure and temperature. Moreover, its potential application of the system as a sensor skin was demonstrated by mounting the flexible sensor system on a prosthetic hand. Our study exhibits a prospective application of using BTO ceramic for flexible self-powered multi-functional coupled sensor systems.

Results and Discussion

Fabrication and characterization of the device

Fig. 1A is a schematic of the sensor system that acts as a wearable electronic device which can sense light, temperature and pressure signals form the external environment. The multilayered design layout and the corresponding fabrication process of the sensor system is presented in Fig. 1B. Transparent ITO and Ag electrodes were deposited on the upper and bottom surfaces of the BTO ceramic wafers, respectively. Subsequently, the BTO ceramic wafer array was encapsulated in PDMS. Schematics of the final fabricated BTO-PDMS device and sensor system under light illumination are shown in fig. S1A and S1B, respectively. Fig. 1C and fig. S1C display the morphology of the BTO nanoparticles with a diameter of approximately 50-100 nm, which were used to fabricate BTO ceramic wafers. As demonstrated in fig. S1D, the thickness of the manufactured BTO ceramic wafer after undertaking the processing technologies of dry pressure sintering, polarization and sanding is approximately 280 μm. The surface, as seen in fig. S1E and 1F, and cross-sectional morphology, Fig. 1D and S1G, of the BTO ceramic wafer indicate that the prepared ceramics possess a highly dense microstructure, and the grain size is less than 5 μm. X-ray diffraction (XRD) patterns in fig. S1H indicate that the BTO nanoparticles after being calcined at 1200 ˚C have an orthorhombic phase. Fig. 1E and Fig.1G present images of the fabricated BTO-PDMS nanogenerator and sensor system with dimensions of 50×15×1 mm and 50×50×1 mm, respectively. As demonstrated in Fig. 1F and 1H, they exhibit good flexibility when subjected to mechanical deformation.

Output performance of the nanogenerators

The output performance of the fabricated device when stimulated independently by light, pressure and temperature were systematically investigated and the data is summarized in Fig. 2. Fig. 2A illustrates the output current signals of the device under periodic illumination by light of a 405 nm wavelength, where the output current increases with an increase in light intensity. The

short-circuit current exhibits a large increase from 3.7 nA to 21.6 nA on increasing the light intensity from 8.39 mW/cm^2 to 83.2 mW/cm^2. Since heat is generated during illumination, the output current signals also exhibits a pyroelectric peak, which also increases with an increase in light intensity. The output voltage signals of the device under the light illumination can also be observed in fig. S2A, which exhibit the same trends as the output current. To confirm that the signals in Fig. 2A and fig. S2A are generated by the BTO-PDMS nanogenerator, the fabricated device was forwardly and reversely connected to the measurement system, with positive and negative signals observed when turning on the light see fig. S2C and fig. S2D. The corresponding negative signals at reversed connection indicate that the measured signals were generated by the polarized BTO-PDMS nanogenerator.

The output piezoelectric current signals of the BTO-PDMS nanogenerator exhibits a clear increase from 6.5 nA to 21.2 nA as the magnitude of the alternating pressure increases from 7.6 kPa to 33.7 kPa, as demonstrated in Fig. 2B. To further confirm that the output signals originate from the direct piezoelectric effect, the output voltage signals of the BTO-PDMS device at forward connection and reversed connection to the measurement system under repeated pressure cycling were measured, see fig. S2D. Linear fitting results of the output current of the device under different pressures show that the trend of an increase in current with pressure can be divided into two segments, whose slopes K_1 and K_2 are 0.91 and 0.29, respectively; see fig. S2E. Fig. 2C and fig. S2F display the output current signals for BTO-PDMS nanogenerator when subjected to a range of temperature variations only. When heated with a temperature variation of ΔT = 35.1 K, the output current is approximately 15.7 nA (Fig. 2C), whereas the output current was approximately 14.3 nA when cooled with a temperature variation of ΔT = -19.5 K (fig. S2F). The temperature-time curves and the corresponding output voltage signals of the nanogenerator under different temperature variation are presented fig. S3A, S3B, S3D and S3E, which show that the output voltage signals of the device increase with an increase of heating or cooling temperature variations. The corresponding infrared images of the device at the different temperature variations can be observed by an infrared thermometer, as shown in fig. S3C.

To clearly demonstrate the output performance of the fabricated device, the output current under a range light intensities, pressures and temperature variations are summarized in Figs. 2D-2F. The result shows that the output current signals of the device increase monotonically with light intensity, pressure and temperature. The output power of the nanogenerator was systematically investigated by connecting the sensor in series with different resistances, as depicted in fig. S4. The maximum output power was obtained at a matched loading resistance with respect to the photovoltaic effect, piezoelectric effect and pyroelectric effect. The maximum output power for

the photovoltaic mode of operation is ~ 0.81 nW (33.7 kPa) located at a loading resistance of 4.0 MΩ (83.2 mW/cm^2); for the piezoelectric mode the maximum output power is ~ 0.19 nW at a loading resistance of 0.9 MΩ; and for the pyroelectric mode the maximum output power is ~ 22.4 nW (ΔT = 39.1 K) and 25.5 nW (ΔT = -19.5 K) at loading resistances of 200 MΩ and 260 MΩ, respectively. All output current signals decrease with an increase in load resistance since the system is approaching open circuit conditions.

As a key parameter of a sensor, the response speed of the fabricated device was investigated in detail and shown in figs. S5A-5C. The response time and recovery time of the ITO/BTO/Ag structure to illumination by light, pressure and heating was calculated between 10% and 90 % of the maximum current signal, respectively. When illuminated by light with a 405 nm wavelength, fig. S5A, the response time and the recovery time are approximately 0.68 s and 0.56 s. For the piezoelectric effect, fig. S5B, the device exhibits a fast pressure response time and recovery time of 0.03 s and 0.02 s respectively. As shown in fig. S5C, the device exhibits a more moderate temperature response time of 2.06 s and recovery time of 32.63 s, respectively due to the slower speed associated with heat transfer. In addition, the stabilities of the fabricated BTO-PDMS nanogenerator under the application of cyclic heating and cyclic pressures were tested, respectively. As demonstrated in Fig. S6, the consistent output current signals indicate the excellent stability of the fabricated device to operating conditions.

Multi-coupled effects performance of the nanogenerators

Due to the multi-functional properties of the BTO-PDMS nanogenerator, it is of interest to investigate the mutual influence between the photovoltaic effect, piezoelectric effect and pyroelectric effect. Figs. 3A and B present the output current signals of the device under the application of independent heating (ΔT = 35.1 K) or cooling (ΔT = -19.5 K) temperature variations, and the application of combined temperature variations and light illumination of different intensities (8.39 to 83.2 mW/cm^2). The result shows that the coupled current of the device under the action of a combined cooling temperature variation (ΔT = -19.5 K) and illumination (83.2 mW/cm^2) is 36.1 nA. As a result of the coupling between the ferroelectric effect and photovoltaic effect, when the temperature variation is ΔT = 35.1 K, the coupled current is reduced to 15.1 nA. The output current signals of the device under the combined application of a range of heating/cooling temperature variations and illumined with light of different intensities is shown in figs. S7 and S8, respectively. To compare the change of current (I_c) under different conditions, the output current signals of the device in Fig. 3A, Fig. 3B, fig. S7 and fig. S8 are summarized in Fig. 3C. The current signal increases monotonically with light intensity for a specific temperature variation (ΔT). It is worth highlighting that the slopes of the

fitted current-light intensity lines decrease with an increase of ΔT and detailed information can be found in Table S1. A heating temperature variation results in the weakening of the output current signals and cooling temperature variation can be utilized to enhance the output current signals of the device, which can be explained by the pyro-phototronic effect (27). For ferroelectric BTO materials, the spontaneous polarization can be enhanced when it is cooled, resulting in the increase of the internal electric field. As a result, the light-induced electrons and holes can be separated more effectively as compared with that of a higher temperature condition. Figs. S9 and S10 display the output voltage signals of the device under the simultaneous application of a temperature change (ΔT) and illumination with light of different intensities. To compare voltage signals of the device under the different condition, the output voltage is further summarized in fig. S17A and shows a clear increase with increasing cooling temperature and decrease with increasing heating temperature variations under a certain light intensity.

Figs. 3D, 3E, S11and S12 illustrate the output current signals of the device under the application of individual heating and cooling temperature variations, simultaneous application of temperature variations and different alternating pressures from 7.6 kPa to 33.7 kPa. When the heating temperature variation is ΔT = 35.1 K, the coupled currents of the device under 7.6 kPa and 33.7 kPa are 4.1 nA and 10.0 nA, respectively. When the cooling temperature variation is ΔT = -19.5 K, the coupled currents of the device under 7.6 kPa and 33.7 kPa are 11.1 nA and 34.8 nA, respectively. By comparison, a heating temperature variation can be utilized to weaken the output current signals and cooling temperature variation can be utilized to enhance the output current signals (I_f) of the device, as presented in Fig. 3F. Moreover, the slopes of the currents linear fitting equations increase with an increase of cooling temperature and decreases with the increase of heating temperature variations, respectively, as displayed in Table S2.

Figs. 3g, 3h, S13 and S14 display the output current signals of the device under the different illumination intensities, simultaneous light illumination and heating/cooling with different temperature variations from 35.1 K to -19.5 K. The coupled currents of the device under the simultaneous light illumination (8.39 mW/cm^2) and temperature variations (35.1 K or -19.5 K) are 2.2 nA and 7.8 nA. The corresponding coupled currents under the light intensity of 83.2 mW/cm^2 are 14.2 nA and 102.6 nA, respectively. The results indicate that a cooling temperature variation can be utilized to enhance the output current signals of the device under the same light intensity which can be attributed to the pyro-phototronic effect. Moreover, the spontaneous polarization in BTO can be decreased when it was heated, resulting in the decrease of the internal electric filed. As a result, it is more difficult for effective separation of electrons and holes as compared to the no heating condition.

The absolute values of the output currents and linear fitting gradient increases with an increase of light intensity, see Fig. 3I and Table S3. The changes of the corresponding voltage signals of the device were consistent with the current, as demonstrated in figs. S15, S16 and S17B. Moreover, we measured the coupled current of the device under the application of simultaneous illumination by light and alternating pressure, as displayed in figs. S18 and S19. The results show that the coupled current is larger than the individual photocurrent. Moreover, the coupling current increases with an increase of light intensity. Under a cooling temperature variation of ΔT = -19.5 K, the coupled current and voltage of the device under simultaneous cooling temperature variation and light illumination (8.39 mW/cm^2) was enhanced by ~ 47.5 % and ~ 155 % when compared with the current and voltage of the device under individual light illumination, see figs. S20A and S20B. Under a light intensity of 83.2 mW/cm^2, the coupled current of the device under simultaneous light illumination and pressure (7.6 kPa) was enhanced by ~ 387.3 % when compared with the current of the device under individual light illumination, see fig. S20). The coupled current of the device under simultaneous cooling temperature variation (ΔT = -19.5 K) and pressure (7.6 kPa) was enhanced by ~ 71.1 % when compared with the current of the device under individual cooling, see fig. S20D. Under a light intensity of 83.2 mW/cm^2, the output current and voltage of the device under simultaneous light illumination and cooling temperature variation (ΔT = -19.5 K) can be enhanced by about 375.0 % and 56.3 % when compared with the current and voltage of the device under individual light illumination, respectively (figs. S20E and S20F).

Output performance of the self-powered multi-functional coupled sensor systems

In order to expand the application of the device, we designed a self-powered multi-functional coupled sensor system by fabricating a 3×3 matrix of BTO ceramic wafers. Figs. S21A-C present the current-time curves of all the channels of the sensor system under the application of a cyclic pressure of 33.7 kPa, temperature variations with a heating temperature change of ΔT = 35.1 K and a cooling temperature change of ΔT = -19.5 K, respectively. The result indicated that the nine channels of the 3 x 3 sensor system show good output stability, and each channel presented similar current signals as the pressure or temperature variations were turned on and off. By illuminating with 405 nm light to specific channels of the fabricated sensor system through a mask, the current signals could be observed on the mapping figure for the illuminated channels. Figs. 4A-C show clear "Z", "L" and "T" shapes in the current output on the mapping image when illuminated with 405 nm light with an of intensity of 83.2 mW/cm^2 on the sensor system through a mask with "Z", "L" and "T" shape on it. The corresponding output current of the sensor system

are displayed in figs. S22A-C. From the diagram, it can be seen that there is a steady current signal of ~ 20 nA in the illuminated channels, but no current signals in the blocked channels.

Mapping images of the sensor system under the simultaneous application of heating and pressure or cooling and pressure through a shape of "T" are demonstrated in Figs. 4D and 4E, respectively. It can be clearly seen from the images that the coupled current between cooling and pressure is larger than heating and pressure at the same pressure, which is also illustrated by Figs.4G and 4H. Fig. 4F and fig. S23A show the mapping output current and current-time curve of the sensor system under the simultaneous 405 nm illumination and pressure through a shape of "T". Comparing Fig. 4C with Fig. 4F, it can be seen that the photovoltaic-piezoelectric coupled effect can be utilized to enhance the output current signals of the sensor system. The output current-time curves and mapping output currents of the sensor system under the simultaneous heating or cooling temperature variations and light illumination through a sharp of "T" as displayed in figs. S23B, S23C, S23D and S23E, respectively. The results show that a combination of cooling-light illumination can enhance the current signals of the sensor system, while heating-light illumination can weaken the signal, for the reasons described above.

Application of the flexible and self-powered multi-functional coupled sensor systems

The fabricated sensor system can be worn on a prosthetic hand to detect light, pressure and temperature variations. Fig. 5A presents an optical image of the sensor system attached to a prosthetic hand, demonstrating high flexibility. Figs. 5B and C show images of the sensor system attached to a prosthetic hand under illumination by 405 nm light and fingertip pressure. The output current signals of the channels 2 and 3 were measured, as illustrated in Fig. 5D and fig. S24A, respectively. The output voltage signals of channel 2 and 3 of the sensor system under different finger pressures are displayed in fig. S24B and the above results indicate that the system can be used to detect the magnitude of light intensity and pressure. Fig.5E shows an image of ice placed on the sensor system, where the size of the ice exactly covers the area of channel 2. A photograph and infrared image of the sensor system under the combined action of 405 nm illumination and ice cooling is presented in Figs. 5F and 5G, respectively. The corresponding output current signals of channel 2 of the sensor system under the individual 405 nm illumination is approximately 20.2 nA, the simultaneous light illumination and ice cooling increase to 36.8 nA (Fig. 5H). The output current of channel 2 under simultaneous light illumination and ice cooling is calculated to increase by 82.2% compared to individual light illumination. Therefore, the fabricated multifunction coupled sensor system can be successfully implemented for the measurement of light illumination, pressure and temperature changes in the environment.

Conclusion

In summary, we have designed a unique one-structure-based multi-effect coupled nanogenerator based on BTO ceramic wafers encapsulated in PDMS. When compared with the individual photovoltaic effect, piezoelectric effect and pyroelectric effect, coupled effects are displayed to have a much larger electrical output. Under a light intensity of approximately 83.2 mW/cm^2, the coupled current of the device under simultaneous light illumination and pressure (7.6 kPa) can be enhanced by ~ 387.3 % when compared with the current of the device under individual light illumination. By applying a cooling temperature change of ΔT = -19.5 K, the output current signals can be enhanced by over 375.0 % under a light intensity of 83.2 mW/cm^2. Our results reveal the role of coupled effect in BTO nanogenerator and sensor systems, which has potential applications in improving the output performance of coupled nanogeneratosr based on ferroelectric materials such as hybrid nanogenerators and multi-functional coupled sensors. The nanogenerator was then applied as a self-powered multi-functional coupled sensor system for monitoring variations in light, pressure and temperature. In contrast to conventional multi-function sensor systems, a single pixel of our sensor system is able to simultaneously detect light, pressure and temperature variation which can significantly improve sensor integration level and reduce cost. In addition, when mounted on a prosthetic hand, the flexible sensor systems can detect the distribution of light, pressure and temperature variations, exhibiting potential applications as an electronic sensor skin.

Materials and Methods

Preparation of BTO ceramic wafers

A mass of 0.3 g of BTO nanoparticles was thoroughly mixed with several drops of 2 wt.% polyvinyl alcohol (PVA) binder. The obtained fine powders were then transferred to stainless steel mould and compacted into wafers with a diameter of 10 mm under 2.5 MPa. Subsequently, the BTO wafers were sintered at 650 $^{\circ}C$ for 1 h to eliminate the PVA binder, and then sintered at 1200 $^{\circ}C$ for 2 h to obtain BTO ceramic wafers.

Fabricationsof nanogenerators and sensor systems

A thin layer of Ag was sputtered on the two surfaces of the obtained BTO ceramic wafers using a DC magnetron sputtering system (100 W, 30 min) to act as an electrode. The Ag/BTO/Ag devices were then poled for 30 min under an applied electric field of 2.3 kV/mm in a silicone oil bath at room temperature. Finally, by removing one Ag electrode and polishing the BTO ceramic wafer to approximately 280 μm, an ITO electrode was deposited on the polished side of BTO wafer by RF magnetron sputtering for 15 min using a power of 150 W. For the structural layers,

the molds (sizes: 50×15×1 mm and 50×50×1 mm) with acrylic sheets were manufactured by processing them as different parts using a laser cutter and bonding the parts together with epoxy. The liquid silicone rubber was obtained by mixing a Sylgard 184 base with curing agents at a mass ratio of 10:1 in a beaker. The liquid silicone was then poured inside the molds with BTO ceramic wafers installed in the center and cured at 90 °C for 1 h. The nanogenerator (NG) was obtained by encapsulating a BTO ceramic wafer in PDMS (mold size: 50×15×1 mm). The 3×3 matrix flexible sensor systems were assembled by encapsulating nine BTO ceramic wafers in PDMS (mold size: 50×50×1 mm).

Characterization and measurements

SEM images were determined using field emission scanning electron microscopy (Hitachi SU8020). The crystal structure of BTO nanoparticles was identified by an X-ray diffractometer (Panalytical X'pert^3 powder), using Cu Kα radiation. The heating and cooling temperature variations for BTO-PDMS NG and sensor system were achieved by a thermoelectric module positioned below the device, and temperature was monitored using an infrared thermometer (Optris PI400). The illumination intensity was measured by power meter (Nova Ⅱ Display ROHS) and the applied pressure was determined using a digital dynamometer (ZTA-DPU-50 N). The output current and voltage signals of the nanogenerator and sensor system were measured by a 2611B system source meter. The output voltages of the device were measured under a load resistance of approximately 100 MΩ.

Supplementary Materials

Supplementary materials for this article is available at http://advances.sciencemag.org/cgi/content/full/

fig. S1. (**A,B**) Schematic diagrams of the fabricated BTO-PDMS device (A) and sensor systems (B) under light illumination. (**C**) SEM image of the BTO nanoparticles with the low magnification. (**D**) Thickness of the BTO ceramic wafer observed by SEM. (**E,F**) Surface SEM images of BTO ceramic wafer with the low (E) and high (F) magnifications. (**G**) Cross-sectional SEM image of BTO ceramic wafer with the low magnification. (**H**) X-ray diffraction patterns of BTO nanoparticles before and after calcination.

fig. S2. (**A**) Measured output voltage signals for BTO-PDMS device under 405 nm illumination with different intensities from 8.39 to 83.2 mW/cm^2. (**B,C**) Measured output voltage (B) and current signals (C) of the BTO-PDMS device at forward connection and reversed connection to the measurement system by repeatedly light illumination (83.2 mW/cm^2). (**D**) Measured output

voltage signals of the BTO-PDMS device at forward connection and reversed connection to the measurement system by repeatedly pressure (33.7 kPa). (**E**) Measured output currents and its linear fitting curves of the fabricated device under different pressure. (**F**) Measured output current signals for BTO-PDMS device under different cooling temperatures.

fig. S3. (**A**) The cyclic change in temperature of the fabricated device in the different heating conditions. (**B**) Measured voltage signals of the device under the corresponding temperature variations in a. (**C**) Infrared images of the device at the different heating (top) and cooling (bottom) temperature variations. (**D**) The cyclic change in temperature of the fabricated device in the different cooling conditions. (**E**) Measured voltage signals of the device under the corresponding temperature variations in D.

fig. S4. (**A-D**) Measured output currents and calculated output powers of the BTO-PDMS device regarding to photovoltaic effect, piezoelectric effect and pyroelectric effect on loading resistances under 405 nm illumination (**A**, 83.2 mW/cm^2), pressure (**B**, 33.7 kPa), heating (**C**, ΔT=35.1 K) and cooling (**D**, ΔT=-19.5 K).

fig. S5. (**A-C**) Response and recovery time acquired from I-t curves of the device under 405 nm illumination (**A**, 83.2mW/cm^2), pressure (**B**, 33.7 kPa) and heating (**C**, ΔT=35.1 K).

fig. S6. (**A, B**) Measured output current signals (A) of the device under cyclic heating (ΔT=35.1 K) for 600 min, where the enlarged curve is illustrated in B. (**C, D**) Measured output current signals (C) of the device under cyclic pressure (33.7 kPa) for 200 min, where the enlarged curve is illustrated in D.

fig. S7. (**A**) Measured output current signals of the device under the individual heating (ΔT=9.1 K) temperature variations and the simultaneous temperature variations and light illumination with different intensities from 8.39 to 83.2 mW/cm^2. (**B**) Measured output current signals of the device under the individual heating (ΔT=13.9 K) temperature variations and the simultaneous temperature variations and light illumination with different intensities from 8.39 to 83.2 mW/cm^2.

fig. S8. (**A**) Measured output current signals of the device under the individual cooling (ΔT=-8.1 K) temperature variations and the simultaneous temperature variations and light illumination with different intensities from 8.39 to 83.2 mW/cm^2. (**B**) Measured output current signals of the device under the individual cooling (ΔT=-11.5 K) temperature variations and the simultaneous temperature variations and light illumination with different intensities from 8.39 to 83.2 mW/cm^2.

fig. S9. (**A**) Measured output voltage signals of the device under the individual heating (ΔT=9.1 K) temperature variations and the simultaneous temperature variations and light illumination with different intensities from 8.39 to 83.2 mW/cm^2. (**B**) Measured output voltage signals of the device under the individual heating (ΔT=13.9 K) temperature variations and the simultaneous

temperature variations and light illumination with different intensities from 8.39 to 83.2 mW/cm^2. (**C**) Measured output voltage signals of the device under the individual heating (ΔT=35.1 K) temperature variations and the simultaneous temperature variations and light illumination with different intensities from 8.39 to 83.2 mW/cm^2.

fig. S10. (**A**) Measured output voltage signals of the device under the individual cooling (ΔT=-8.1 K) temperature variations and the simultaneous temperature variations and light illumination with different intensities from 8.39 to 83.2 mW/cm^2. (**B**) Measured output voltage signals of the device under the individual heating (ΔT=-11.5 K) temperature variations and the simultaneous temperature variations and light illumination with different intensities from 8.39 to 83.2 mW/cm^2. (**C**) Measured output voltage signals of the device under the individual heating (ΔT=-19.5 K) temperature variations and the simultaneous temperature variations and light illumination with different intensities from 8.39 to 83.2 mW/cm^2.

fig. S11. (**A**) Measured output current signals of the device under the individual heating (ΔT=9.1 K) temperature variations and the simultaneous temperature variations and different pressures from 7.6 to 33.7 kPa. (**B**) Measured output current signals of the device under the individual heating (ΔT=13.9 K) temperature variations and the simultaneous temperature variations and different pressures from 7.6 to 33.7 kPa. (**C**) Measured output current signals of the device under the individual heating (ΔT=20.1 K) temperature variations and the simultaneous temperature variations and different pressures from 7.6 to 33.7 kPa. (**D**) Measured output current signals of the device under the individual heating (ΔT=26.8 K) temperature variations and the simultaneous temperature variations and different pressures from 7.6 to 33.7 kPa.

fig. S12. (**A**) Measured output current signals of the device under the individual cooling (ΔT=-8.1 K) temperature variations and the simultaneous temperature variations and different pressures from 7.6 to 33.7 kPa. (**B**) Measured output current signals of the device under the individual cooling (ΔT=-11.5 K) temperature variations and the simultaneous temperature variations and different pressures from 7.6 to 33.7 kPa. (**C**) Measured output current signals of the device under the individual cooling (ΔT=-14.4 K) temperature variations and the simultaneous temperature variations and different pressures from 7.6 to 33.7 kPa. (**D**) Measured output current signals of the device under the individual cooling (ΔT=-16.9 K) temperature variations and the simultaneous temperature variations and different pressures from 7.6 to 33.7 kPa.

fig. S13. (**A**) Measured output current signals of the device under the illumination intensities of 8.39 mW/cm^2 and the simultaneous light illumination and heating/cooling with different temperature variations from 35.1 to -19.5 K. (**B**) Measured output current signals of the device

under the illumination intensities of 27.0 mW/cm^2 and the simultaneous light illumination and heating/cooling with different temperature variations from 35.1 to -19.5 K. (**C**) Measured output current signals of the device under the illumination intensities of 42.5 mW/cm^2 and the simultaneous light illumination and heating/cooling with different temperature variations from 35.1 to -19.5 K.

fig. S14. (**A**) Measured output current signals of the device under the illumination intensities of 63.1 mW/cm^2 and the simultaneous light illumination and heating/cooling with different temperature variations from 35.1 to -19.5 K. (**B**) Measured output current signals of the device under the illumination intensities of 66.8 mW/cm^2 and the simultaneous light illumination and heating/cooling with different temperature variations from 35.1 to -19.5 K.

fig. S15. (**A**) Measured output voltage signals of the device under the illumination intensities of 8.39 mW/cm^2 and the simultaneous light illumination and heating/cooling with different temperature variations from 35.1 to -19.5 K. (**B**) Measured output voltage signals of the device under the illumination intensities of 20.7 mW/cm^2 and the simultaneous light illumination and heating/cooling with different temperature variations from 35.1 to -19.5 K. (**C**) Measured output voltage signals of the device under the illumination intensities of 27.0 mW/cm^2 and the simultaneous light illumination and heating/cooling with different temperature variations from 35.1 to -19.5 K. (**D**) Measured output voltage signals of the device under the illumination intensities of 42.5 mW/cm^2 and the simultaneous light illumination and heating/cooling with different temperature variations from 35.1 to -19.5 K.

fig. S16. (**A**) Measured output voltage signals of the device under the illumination intensities of 63.1 mW/cm^2 and the simultaneous light illumination and heating/cooling with different temperature variations from 35.1 to -19.5 K. (**B**) Measured output voltage signals of the device under the illumination intensities of 66.8 mW/cm^2 and the simultaneous light illumination and heating/cooling with different temperature variations from 35.1 to -19.5 K. (**C**) Measured output voltage signals of the device under the illumination intensities of 83.2 mW/cm^2 and the simultaneous light illumination and heating/cooling with different temperature variations from 35.1 to -19.5 K.

fig. S17. (**A**) Comparison of the measured output voltage signals of the device under the simultaneous heating/cooling with different temperature variations and light illumination with different intensities from 8.39 to 83.2 mW/cm^2. (**B**) Comparison of the measured output voltage signals of the device under the simultaneous light illumination and heating/cooling with different temperature variations from 35.1 to -19.5 K. (**C**) Comparison of the measured output voltage

signals of the device under the simultaneous light illumination and heating/cooling with different pressures from 7.6 to 33.7 kPa.

fig. S18. (**A-D**) Measured output current signals of the device under the individual light illumination with intensities of 8.39 (A), 20.7 (B), 27.0 (C) and 42.5 mW/cm^2 (D) and the simultaneous light illumination and different pressures from 7.6 to 33.7 kPa.

fig. S19. (**A-C**) Measured output current signals of the device under the individual light illumination with intensities of 63.1 (A), 66.8 (B) and 83.2 mW/cm^2 (C) and the simultaneous light illumination and different pressures from 7.6 to 33.7 kPa.

fig. S20. (**A,B**) Current (A) and voltage (B) enhanced ratios under the simultaneous temperature variations and light illumination with different intensities due to the pyroelectric-photovoltaic coupled effect. (**C**) Current enhanced ratios under the simultaneous light illumination and pressures due to the photovoltaic-piezoelectric coupled effect. (**D**) Current enhanced ratios under the simultaneous temperature variations and pressures due to the pyroelectric -piezoelectric coupled effect. (**E,F**) Current (E) and voltage (F) enhanced ratios under the simultaneous light illumination and temperature variations due to the photovoltaic-pyroelectric coupled effect.

fig. S21. (**A**) Measured output current signals of the sensor system under pressure of 33.7 kPa. (**B,C**) Measured output current signals of the sensor system under temperature variations with a heating temperature change of 35.1 K (B) and a cooling temperature change of -19.5 K (C).

fig. S22. (**A-C**) Measured output currents of the self-powered multi-functions coupled sensor system under 405 nm illumination through shapes of “Z” (A), “L” (B) and “T” (C).

fig. S23. (**A**) Measured output currents of the sensor systems under the simultaneous light illumination (83.2 mW/cm^2) and pressure (33.7 kPa) through a sharp of "T". (**B**) Measured output currents of the sensor system under the simultaneous heating (ΔT=35.1 K) and light illumination (83.2 mW/cm^2) through a sharp of "T". (**C**) Measured output currents of the sensor system under the simultaneous cooling (ΔT=-19.5 K) and light illumination (83.2 mW/cm^2) through a sharp of "T". (**D,E**) Demonstration of the mappings output current of the sensor system under the simultaneous heating and light illumination (D) or cooling and illumination (E) through a shape of "T".

fig. S24. (**A**) Measured output current signals of channel 3 of the sensor systems under 405 nm illumination and finger pressure. (**B**) Measured output voltage signals of channels 2 and 3 of the sensor system under the different finger pressure.

Table S1. The slopes of the currents linear fitting equations in Fig. 3C.

Table S2. The slopes of the currents linear fitting equations in Fig. 3F.

Table S3. The slopes of the currents linear fitting equations in Fig. 3I.

References and Notes

1. K. Domanski, E. A. Alharbi, A. Hagfeldt, M. Grätzel, W. Tress, Systematic investigation of the impact of operation conditions on the degradation behaviour of perovskite solar cells. *Nat. Energy* **3**, 61-67 (2018).
2. G. E. Eperon, T. Leijtens, K. A. Bush, R. Prasanna, T. Green, J. T.-W. Wang, D. P. McMeekin, G. Volonakis, R. L. Milot, R. May, A. Palmstrom, D. J. Slotcavage, R. A. Belisle, J. B. Patel, E. S. Parrott, R. J. Sutton, W. Ma, F. Moghadam, B. Conings, A. Babayigit, H.-G. Boyen, S. Bent, F. Giustino, L. M. Herz, M. B. Johnston, M. D. McGehee, H. J. Snaith, Perovskite-perovskite tandem photovoltaics with optimized bandgaps. *Science* **354**, 861-865 (2016).
3. Z. Xiao, Y. Yuan, Y. Shao, Q. Wang, Q. Dong, C. Bi, P. Sharma, A. Gruverman, J. Huang, Giant switchable photovoltaic effect in organometal trihalide perovskite devices. *Nat. Mater.* **14**, 193-198 (2015).
4. Z. Li, X. Xu, W. Zhang, X. Meng, Z. Genene, W. Ma, W. Mammo, A. Yartsev, M. R. Andersson, R. A. J. Janssen, E. Wang, 9.0% power conversion efficiency from ternary all-polymer solar cells. *Energ. Environ. Sci.* **10**, 2212-2221 (2017).
5. Y. Yuan, T. Li, Q. Wang, J. Xing, A. Gruverman, J. Huang, Anomalous photovoltaic effect in organic-inorganic hybrid perovskite solar cells. *Sci. Adv.* **3**, 1602164 (2017).
6. Z. L. Wang, J. Song, Piezoelectric nanogenerators based on zinc oxide nanowire arrays. *Science* **312**, 242-246 (2006).
7. C. Chang, V. H. Tran, J. Wang, Y.-K. Fuh, L. Lin, Direct-write piezoelectric polymeric nanogenerator with high energy conversion Efficiency. *Nano Lett.* **10**, 726-731 (2010).
8. K.-I. Park, J. H. Son, G.-T. Hwang, C. K. Jeong, J. Ryu, M. Koo, I. Choi, S. H. Lee, M. Byun, Z. L. Wang, K. J. Lee, Highly-efficient, flexible piezoelectric PZT thin film nanogenerator on plastic substrates. *Adv. Mater.* **26**, 2514-2520 (2014).
9. R. A. Whiter, V. Narayan, S. Kar-Narayan, A scalable nanogenerator based on self-poled piezoelectric polymer nanowires with high energy conversion efficiency. *Adv. Energy Mater.* **4**, 1400519 (2014).
10. J. H. Jung, M. Lee, J.-I. Hong, Y. Ding, C.-Y. Chen, L.-J. Chou, Z. L. Wang, Lead-free $NaNbO_3$ nanowires for a high output piezoelectric nanogenerator. *ACS Nano* **5**, 10041-10046 (2011).

11. S. -H. Shin, Y.-H. Kim, M. H. Lee, J.-Y. Jung, J. Nah, Hemispherically aggregated $BaTiO_3$ nanoparticle composite thin film for high-performance flexible piezoelectric nanogenerator. *ACS Nano* **8**, 2766-2773 (2014).
12. Y. Yang, W. Guo, K. C. Pradel, G. Zhu, Y. Zhou, Y. Zhang, Y. Hu, L. Lin, Z. L. Wang, Pyroelectric nanogenerators for harvesting thermoelectric energy. *Nano Lett.* **12**, 2833-2838 (2012).
13. Q. Leng, L. Chen, H. Guo, J. Liu, G. Liu, C. Hu, Y. Xi, Harvesting heat energy form hot/cold water with a pyroelectric generator. *J. Mater. Chem. A* **2**, 11940-11947 (2014).
14. J. Chun, K. Y. Lee, C.-Y. Kang, M. W. Kim, S.-W. Kim, J. M. Baik, Embossed hollow hemisphere-based piezoelectric nanogenerator and highly responsive pressure sensor. *Adv. Func. Mater.* **24**, 2038-2043 (2014).
15. J.-H. Lee, H. Ryu, T.-Y. Kim, S.-S. Kwak, H.- J. Yoon, T.- H. Kim, W. Seung. S.-W. Kim, Thermally induced strain-coupled highly stretchable and sensitive pyroelectric nanogenerators. *Adv. Energy Mater.* **5**, 1500704 (2015).
16. A. Sultana, Md. M. Alam, T. R. Middya, D. Mandal, A pyroelectric generator as a self-powered temperature sensor for sustainable thermal energy harvesting from waste heat and human body heat. *Appl. Energ.* **221**, 299-307 (2018).
17. S. B. Lang, Pyroelectricity: from ancient curiosity to modern imaging tool. *Phys. Today* **58**, 31-36 (2005).
18. N. Ma, Y. Yang, Enhanced self-powered UV photoresponse of ferroelectric $BaTiO_3$ materials by pyroelectric effect. *Nano Energy* **40**, 352-359 (2017).
19. S. Wada, K. Yako, H. Kakemoto, T. Tsurumi, T. Kiguchi, Enhanced piezoelectric properties of barium titanate single crystals with different engineered-domain sizes. *J. Appl. Phys.* **98**, 014109 (2005).
20. W.-Q. Liao, Y.-Y. Tang, P.-F. Li, Y.-M. You, R.-G. Xiong, Large piezoelectric effect in a lead-free molecular ferroelectric thin film. *J. Am. Chem. Soc.* **139**, 18071-18077 (2017).
21. J. Lim, H. Jung, C. Baek, G.-T. Hwang, J. Ryu, D. Yoon, J. Yoo, K.-I. Park, J. H. Kim, All-inkjet-printed flexible piezoelectric generator made of solvent evaporation assisted $BaTiO_3$ hybrid material. *Nano Energy* **41**, 337-343 (2017).
22. J. Xing, K.-J. Jin, H. Lu, M. He, G. Liu, J. Qiu, G. Yang, Photovoltaic effects and its oxygen content dependence in $BaTiO_{3-\delta}$/Si heterojunctions. *Appl. Phys. Lett.* **92**, 071113 (2008).
23. N. Ma, Y. Yang, Boosted photocurrent in ferroelectric $BaTiO_3$ materials via two dimensional planar-structured contact configurations. *Nano Energy* **50**, 417-424 (2018).

24. H. Fan, C. Chen, Z. Fan, L. Zhang, Z. Tan, P. Li, Z. Huang, J. Yao, G. Tian, Q. Luo, Z. Li, X. Song, D. Chen, M. Zeng, J. Gao, X. Lu, Y. Zhao, X. Gao, J.-M. Liu, Resistive switching and photovoltaic effects in ferroelectric $BaTiO_3$-based capacitors with Ti and Pt top electrodes. *Appl. Phys. Lett.* **111**, 252901 (2017).
25. Bai, Y., Jantunen H. & Juuti J. Energy Harvesting Research: The Road from Single Source to Multisource. *Adv. Mater.* **30**, 1707271 (2018).
26. Bai Y., Tofel, P., Palosaari, J., Jantunen, H., Juuti, J. A Game Changer: A Multifunctional Perovskite Exhibiting Giant Ferroelectricity and Narrow Bandgap with Potential Application in a Truly Monolithic Multienergy Harvester or Sensor. *Adv. Mater.* **29**, 1700767 (2017).
27. Zhang, K., Wang, Z. L., Yang, Y. Enhanced P3HT/ZnO nanowire heterojunction solar cells by pyro-phototronic effect. *ACS Nano* **10**, 10331-10338 (2016).

Acknowledgments

Funding: This work was supported by the National Natural Science Foundation of China (Grant No. 51472055), External Cooperation Program of BIC, Chinese Academy of Sciences (Grant No. 121411KYS820150028), the 2015 Annual Beijing Talents Fund (Grant No. 2015000021223ZK32), the National Key R&D Program of China (Grant No. 2016YFA0202701), Qingdao National Laboratory for Marine Science and Technology (No. 2015ASKJ01), the University of Chinese Academy of Sciences (Grant No. Y8540XX2D2), and the "thousands talents" program for the pioneer researcher and his innovation team, China.

Author contributions: Z.L.W. and Y.Y. conceived of and initiated the project. K.Z. and B.O. carried out the device fabrication and the performance measurement, B.O. created schematic diagrams in the manuscript, K.Z., B.O., C.R.B., Z.L.W. and Y.Y. discussed the results and co-wrote the manuscript.

Competing interests: The authors declare no competing financial interests.

Data and materials availability: All relevant data are available from the authors on request.

Figures

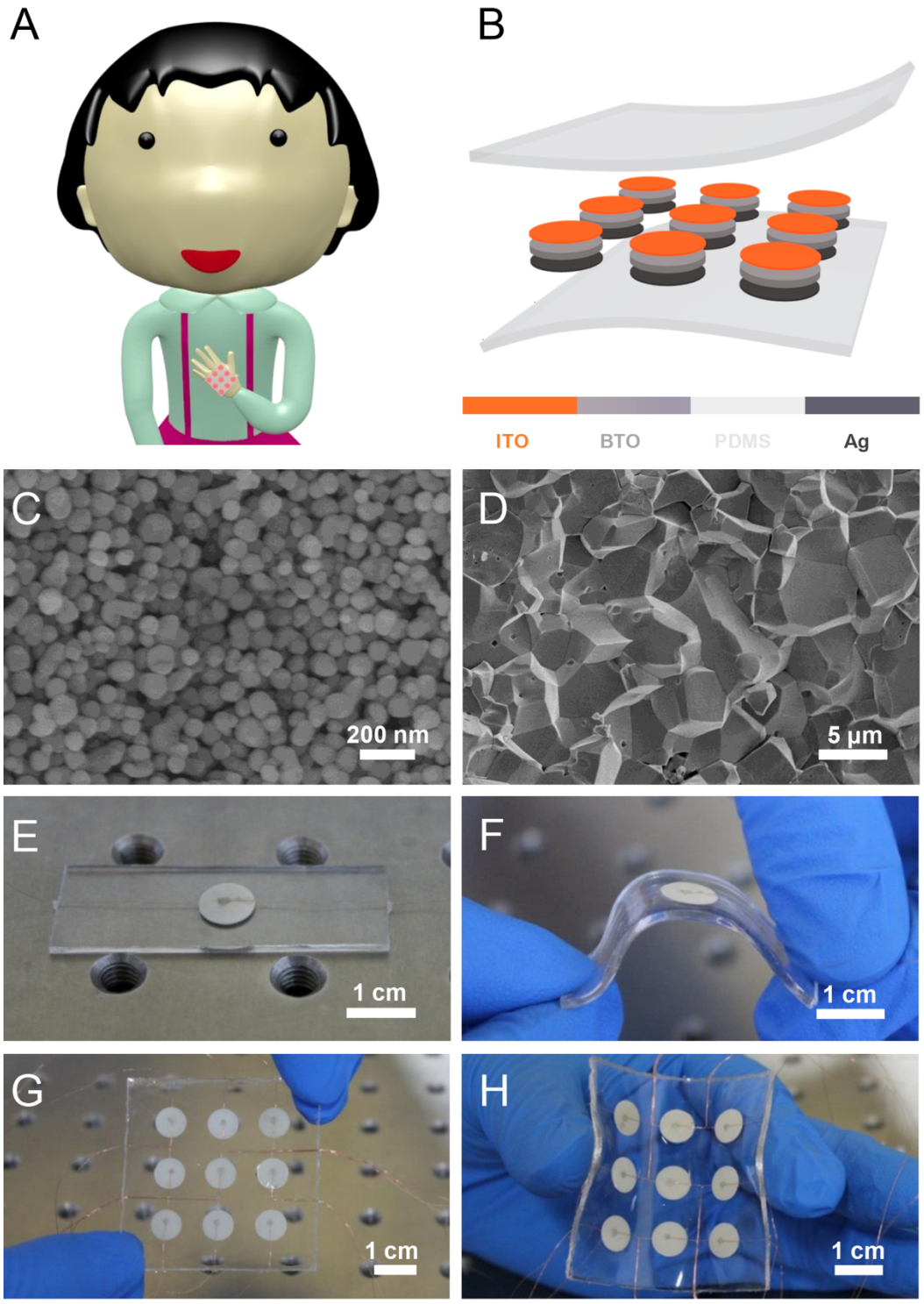

Fig. 1. (**A**) Schematic of the fabricated sensor system for the human body. (**B**) Schematic of the structure of the fabricated sensor system. (**C**) SEM image of BTO nanoparticles. (**D**) Cross-sectional SEM image of BTO ceramic wafer. (**E,F**) Images of flat (E) and flexed (F) BTO-PDMS device. (**G,H**) Images of the flat (G) and flexed (H) sensor system.

TOC

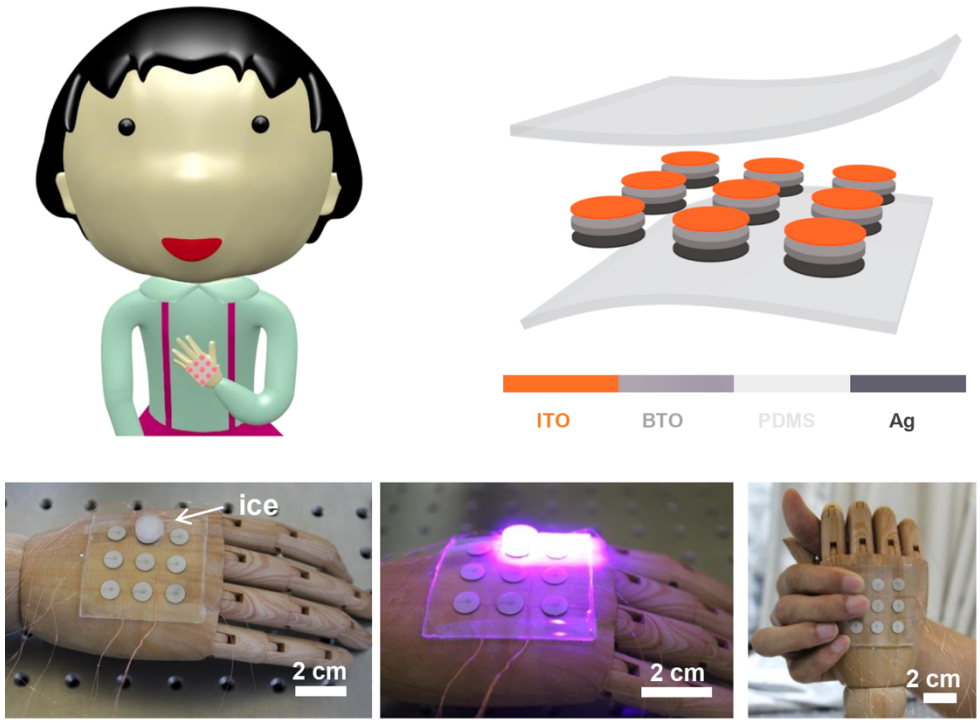

We report a ferroelectric barium titanate (BTO) film-based multi-effect coupled nanogenerator for scavenging light, mechanical, and thermal energies to realize a self-powered multi-functional coupled sensor system without using any external power source. The coupled nanogenerator achieves a clear coupling enhancement with detection sensitivities of 0.42 nA/(mW/cm^2) during illumination by 405 nm light, 1.43 nA/kPa for pressure detection, and -8.85 nA/K for temperature sensing, where both the light and pressure sensing performances have the highest sensitivities under a cooling temperature variation of ~19.5 K and the largest temperature detection sensitivity can be found during strong light illumination of 83.2 mW/cm^2. Moreover, the coupled nanogenerator array can be integrated into flexible forms for tactile pressure, temperature, and light sensors, enabling coupled sensing for electronic skins.